

Magnetic field modulation of high spin hexa-coordinated iron sites to enhance catalytic activity



Hongyao Xue^{a,*}, Jiacheng Wang^{a,1}, He Cheng^{a,1}, Haiqin Zhang^a, Xiyue Li^a, Jianbo Sun^a, Xinyuan Wang^a, Liguo Lin^{a,b,**}, Yixue Zhang^a, Xiaobin Liao^{c,*}, Yan He^{a,*}

^a College of Electromechanical Engineering, Qingdao University of Science and Technology, Qingdao, Shandong 266061, PR China

^b State Key Laboratory of Chemo/Bio-Sensing and Chemometrics, College of Chemistry and Chemical Engineering, Advanced Catalytic Engineering Research Center of the Ministry of Education, Hunan University, Changsha, Hunan 410082, PR China

^c School of Materials Science and Engineering, Wuhan University of Technology, Wuhan, Hubei 430070, PR China

ARTICLE INFO

Keywords:

High spin
Alternating magnetic field
in-situ Raman
Hexa-coordinated iron site
Theory calculations

ABSTRACT

The external alternating magnetic field (AMF) strategy is the most promising research topic to solve the bottleneck of catalyst activity enhancement. However, the mechanism between the arrangement of the spin electrons under the AMF and the catalytic activity enhancement for water splitting is still unclear. Herein, we synthesize $\text{Fe}_3\text{O}_4@\text{CNTs}$ heterostructure as a research model and resolve the mechanism by system theoretical analysis and *in-situ* Raman characterization. The multiple orbital interactions of $\sigma(d_z^2, p_z, s)$ and $\pi(d_{xz}p_x, d_{yz}p_y)$ promote the hexa-coordinated Fe_{oct} for both the reductive HER and oxidative OER processes. The AMF excites the transition from low to high spin configurations of the Fe_{oct} sites, which accelerates charge transfer of unpaired d electrons and optimizes adsorption and desorption interactions to intermediates during the reaction processes, resulting in a significant enhancement of the electrocatalytic activity (HER: 32 mV at 10 mA cm⁻², OER: 179 mV at 100 mA cm⁻²).

1. Introduction

The development of electrocatalysts plays a crucial role in realizing efficient hydrogen production from water-splitting [1,2]. Although Pt/C and RuO₂ are currently the state-of-the-art HER and OER catalysts in commercialization, further progress in this field is limited by their high cost and unsatisfactory stability [3,4]. The spinel oxides with metal cations occupying tetrahedral and octahedral sites are frequently studied as ideal alternatives to commercial precious metal catalysts due to their controllable compositions and structures, abundant coordinatively unsaturated metal center sites and appropriate activities [5]. Among them, Fe₃O₄ has apparent advantages for the HER and OER, but their catalytic performances are still far below expectations due to the low electrical conductivity and sluggish reaction dynamics triggered by high reaction energy barriers [6,7]. To further optimize the catalytic performance, the construction of heterogeneous structures with conductive carbon networks [8–10], heterogeneous atom doping [5,11,12] and ionic defect modulation [13,14] are currently recognized as efficient

methods. However, the exploration of design modifications around the catalyst itself alone to improve the catalytic performance has encountered a bottleneck, making the search for a new strategy one of the most challenging research topics.

Utilizing external field enhancement strategies to boost the catalytic activity, including the integration of external fields such as light, heat, and magnetism, has emerged as a contemporary trend in the field of electrochemistry. Magnetic fields can transfer high-intensity energy to turn the configuration of extra-nuclear spin electrons, thus causing changes in the arrangement, coordination and motion of atoms, molecules as well as ions [15]. Therefore, the application of an external magnetic field during the electrocatalytic reaction can not only further induce changes in the spin state and the degree of orbital hybridization of the magnetic ions, but also activate room-temperature ferromagnetism by changing the spin-orbital configuration, which can significantly affect their catalytic performance [16]. For instance, Yuan and his co-workers found that the oxygen precipitation overpotential of Co@MoS₂ was increased from 317 mV to 250 mV at a current density of

* Corresponding authors.

** Corresponding author at: College of Electromechanical Engineering, Qingdao University of Science and Technology, Qingdao, Shandong 266061, PR China.

E-mail addresses: hongyaofelix@163.com (H. Xue), liguo.lin@126.com (L. Lin), liao.xiaobin@live.com (X. Liao), heyang@qust.edu.cn (Y. He).

¹ These authors contributed equally to this work.

10 mA cm⁻² under the effect of an alternating magnetic field, which suggests that the magnetic field contributes to its catalytic activity enhancement [17]. In addition, magnetic nanocatalysts such as Fe-Co-Ni-P-B [18], Co_{0.8}Mn_{0.2}MOF [19], FeCNI [15], Ni_{56.5}Co₃₅Ti_{8.5} [20], NiFe/NiFeOOH [21], and Gd@MoS₂ [22] similarly showed higher electrocatalytic reaction efficiency and activity. Although the current study demonstrates the enhancement effect of an external magnetic field on catalytic activity, the relationship between the arrangement of spin electrons under the effect of a magnetic field and the HER/OER catalytic activity remains unclear.

Inspired by the above explorations, this work presents an innovative magnetron regulation strategy to enhance the catalytic performance of Fe₃O₄@CNTs heterostructure. Based on density functional theory (DFT) calculations and X-ray absorption spectroscopy (XAS) characterizations, the Fe₃O₄@CNTs heterostructure with higher activity than the pure Fe₃O₄ phase is chosen as the research model for the next work. To deeply investigate the relationship between the arrangement of spin electrons under the magnetic field and the catalytic activity, we first need to clarify the catalytic reaction mechanism. Systematic theoretical analysis and *in-situ* Raman characterization provide systematic insights: 1. Based on the multiple orbital interactions of $\sigma(d_z^2, p_z, s)$ and $\pi(d_{xz}, p_x, d_{yz}, p_y)$, the hexa-coordinated Fe_{oct} sites at the surface exhibit favorability for both the reductive HER and oxidative OER processes; 2. The alternating magnetic field excites the high spin configurations of the Fe_{oct} sites in the Fe₃O₄@CNTs heterostructure. The unpaired *d* electrons yield accelerated charge transfer and optimized adsorption and desorption interactions to intermediates in the reaction processes, thereby significantly enhancing the electrocatalytic activity. Unsurprisingly, its overpotential for HER at a current density of 10 mA cm⁻² decreases from 89 mV to 32 mV after 20 min of applying an alternating magnetic field. In the case of OER, the magnetic field not only accelerates the generation of FeOOH species, but also enhances the adsorption-desorption rate of oxygen-containing intermediates on the surface, which is manifested by the increased activity from 245 mV to 179 mV at a current density of 100 mA cm⁻². This work highlights the utilization of magnetic field excitation as a promising approach to enhance the efficiency of water-splitting technology that is essential for the "dual-carbon" strategy.

2. Experimental details

2.1. Preparation of substrate materials

In this work, nickel foam (0.5 cm × 1.0 cm) is used as the substrate material of the catalyst. Firstly, nickel foam (NF) was immersed in 1.0 mol HCl solution for 5 minutes to remove NiO impurities on the surface, next rinsed three times with deionized water. The processed NF was divided into two categories: the first type was suffered nothing treatment anymore, and the other type was sprayed with self-prepared multi-walled carbon nanotubes (CNTs) solution. Finally, all NFs were placed in an electric blast drying oven and dried at 60 °C.

2.2. Synthesis of Fe₃O₄ and Fe₃O₄@CNTs

Fe₃O₄ and Fe₃O₄@CNTs were synthesized through a convenient one-step hydrothermal method. The synthesis method is as follows: solution A: 0.027 g, 0.189 g, 0.273 g, 1.89 g (0.1 mmol, 0.7 mmol, 1.0 mmol, 7.0 mmol) ferric chloride hexahydrate (FeCl₃·6 H₂O) were dissolved in 14 ml ethylene glycol (C₂H₆O₂), respectively; solution B: 2.88 g sodium acetate (C₂H₃NaO₂) was dissolved in 40 ml of ethylene glycol (C₂H₆O₂). Then solution B were slowly injected into solution A, respectively. Magnetically stirred the mixed solution at room temperature for 90 minutes, next two types of NF were put into the mixed solution. Then they were placed in an electric blast drying oven and heat it up to 200 °C for 480 minutes. After cooling to room temperature, obtained Fe₃O₄/NF and Fe₃O₄@CNTs/NF.

2.3. Characterization

The phase composition was analyzed by X-ray diffraction (XRD; Rigaku MiniFlex-600) and Raman spectrometer (RENISHAW). The specific surface and pore size analysis was measured by BeiShiDe Instrument (3 H-2000PS1 static volume method). The high magnification morphology and structure of the material were characterized by a scanning electron microscope (SEM; HITACHI SU-8010) and a transmission electron microscope (TEM; FEI Tecnai F20). The elemental distribution mapping was scanned by the TEM (FEI Tecnai F20) which is equipped with energy dispersive X-ray (EDX) spectroscopy. The inner shell electron binding energy and chemical shift of the samples were evaluated by X-ray photoelectron spectrometer (XPS; Thermo Scientific K-Alpha). The XAS including X-ray absorption near-edge structure (XANES) and extended X-ray absorption fine structure (EXAFS) of the samples (eV were collected at the SPring-8 14b2, where a pair of channel-cut Fe (311) crystals was used in the monochromator. The storage ring was working at the energy of 8.0 GeV with an average electron current of 99.5 mA.

2.4. Electrochemical measurements

All electrochemical measurements were tested on an electrochemical workstation (ChenHua CHI660E) and were processed with a three-electrode system in 1.0 M KOH solution. The Hg₂Cl₂ electrode and carbon rod were as the reference and counter electrodes, respectively. The linear sweep voltammetry (LSV) measurements were accompanied by a scan rate of 10 mV s⁻¹. Based on the equation: V_{RHE} = V_{Hg2Cl2} + 0.059×pH + 0.2412, the tested potentials vs. Hg₂Cl₂ electrode V_{Hg2Cl2} were rectified to obtain the potentials vs. standard hydrogen electrode (V_{SHE}). The calculations of corresponding Tafel slopes were based on the equation: $\eta = b \cdot \lg(j) + a$ (η is the overpotential, j is the current density, a is the y-intercept and b is the Tafel slope). The compensation resistance of all electrode materials was tested by using the electrochemical impedance spectroscopy (EIS) method with a frequency range of (0.01 Hz to 100 kHz) corresponding to the open circuit voltage. Its durability is evaluated through cyclic voltammetry (CV) and chronopotentiometry measurements 1.0 M KOH solution.

2.5. Density functional theory (DFT) simulations

All the spin-polarized calculations were performed within the Vienna Ab initio Simulation Package (VASP) [23]. Perdew–Burke–Ernzerhof (PBE) functional at the generalized gradient approximation (GGA) was applied to describe the electronic interactions of the studied systems accurately [24]. The Kohn-Sham one-electron states were expanded using the plane wave basis set with an energy cutoff of 500 eV for self-consistent calculations and structural optimizations. The non-bonding interactions between adsorbates and substrate were described via the DFT-D3 method with BJ-damping [25]. The K-point was sampled by the Monkhorst-Pack method with the value of 3×3×1 (0.01 π/Å). The DFT+U method was used to consider the strong electron correlations for Fe in FeOOH and the "U–J" values were 3.5 eV for Fe. The convergence criteria are set as 0.05 eV Å⁻¹ and 1.0×10⁻⁵ eV in force and energy, respectively. We apply the constrained local magnetic moment of 3 to simulate the effect of external magnetic field on the systems.

3. Results and discussion

As revealed in Fig. 1, the surface active Fe sites of the catalysts are the low spin Fe_{oct} with *d*⁵ electronic configurations. The Fe_{oct} shows the unsaturated five-coordinated configuration and has the *d* orbitals within five groups: d_z^2 , d_{xy}^2 , d_{xy} , d_{xz} , and d_{yz} (Figure R1). Consequently, the Fe_{oct} active sites engage in orbital interactions with relevant intermediates, involving the π^*/π interaction of d_{xz} , d_{yz} and p_x , p_y from Fe-3d (d_{xz} and

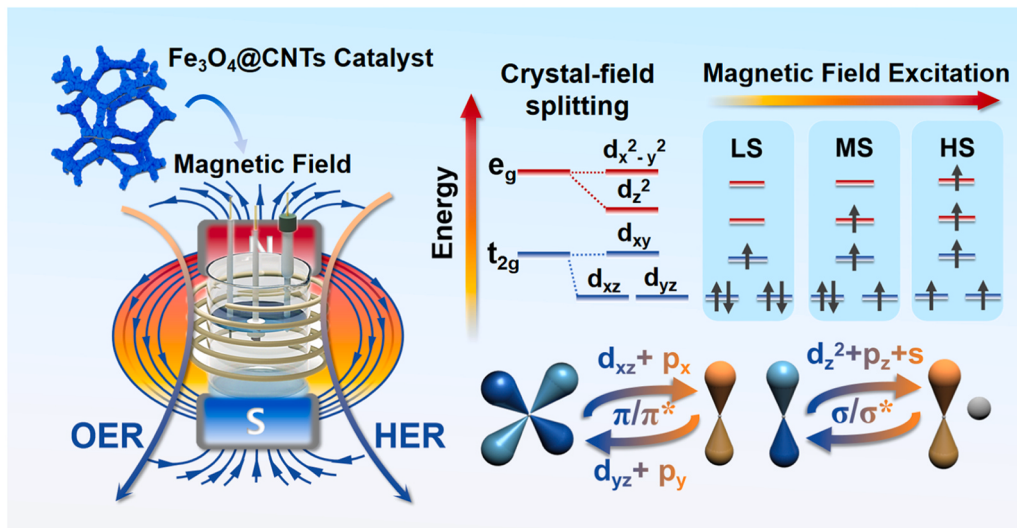


Fig. 1. The magnetron regulation strategy enhances the hydrogen and oxygen evolution activity of $\text{Fe}_3\text{O}_4@\text{CNTs}$ heterostructure.

d_{yz}) and O-2p (p_x and p_y) in oxygen-containing intermediates (O^* , OH^* and OOH^*). The σ^*/σ interaction of d_z^2 , p_z and s orbitals from Fe-3d, O-2p (p_z) and s orbitals in oxygen-containing intermediates (O^* , OH^* and OOH^*), and s orbital from the proton H^* [26]. Unfortunately, the relatively low spin configuration of Fe_{oct} shows limited intrinsic activity for the overall water-splitting reactions. Therefore, we propose the utilization of an external magnetic field to “tune on” the high spin Fe_{oct} and enhance the catalytic activity and electron transfer for boosting the HER and OER processes.

We first apply DFT calculations to investigate in detail the electrocatalytic activities of tetra- and hexa-coordinated Fe sites (Fe_{tet} and Fe_{oct}) in the pure Fe_3O_4 and $\text{Fe}_3\text{O}_4@\text{CNTs}$ (the fully relaxed models are

shown in Figure S2-S3) [27]. The spin-polarized density of states (DOS) plots of pure Fe_3O_4 and $\text{Fe}_3\text{O}_4@\text{CNTs}$ are displayed in Fig. 2a-b. It can be observed that the spin-up and -down in their total DOS are asymmetric, suggesting they are ferromagnetic properties of the samples [17]. Notably, $\text{Fe}_3\text{O}_4@\text{CNTs}$ presents a higher state in the low DOS region close to the Fermi level compared to the pure phase, which implies that the introduction of carbon tubes provides the continuum electron transfer pathway and improves overall electrical conductivity, thus enhancing the efficiency of the electrocatalytic reaction [28]. It is well known that the d -band center represents the degree of electron filling in the d -orbitals, and its value reflects the intrinsic catalytic activity of the catalyst [29]. As shown in Fig. 2c, the d -band center energies of pure

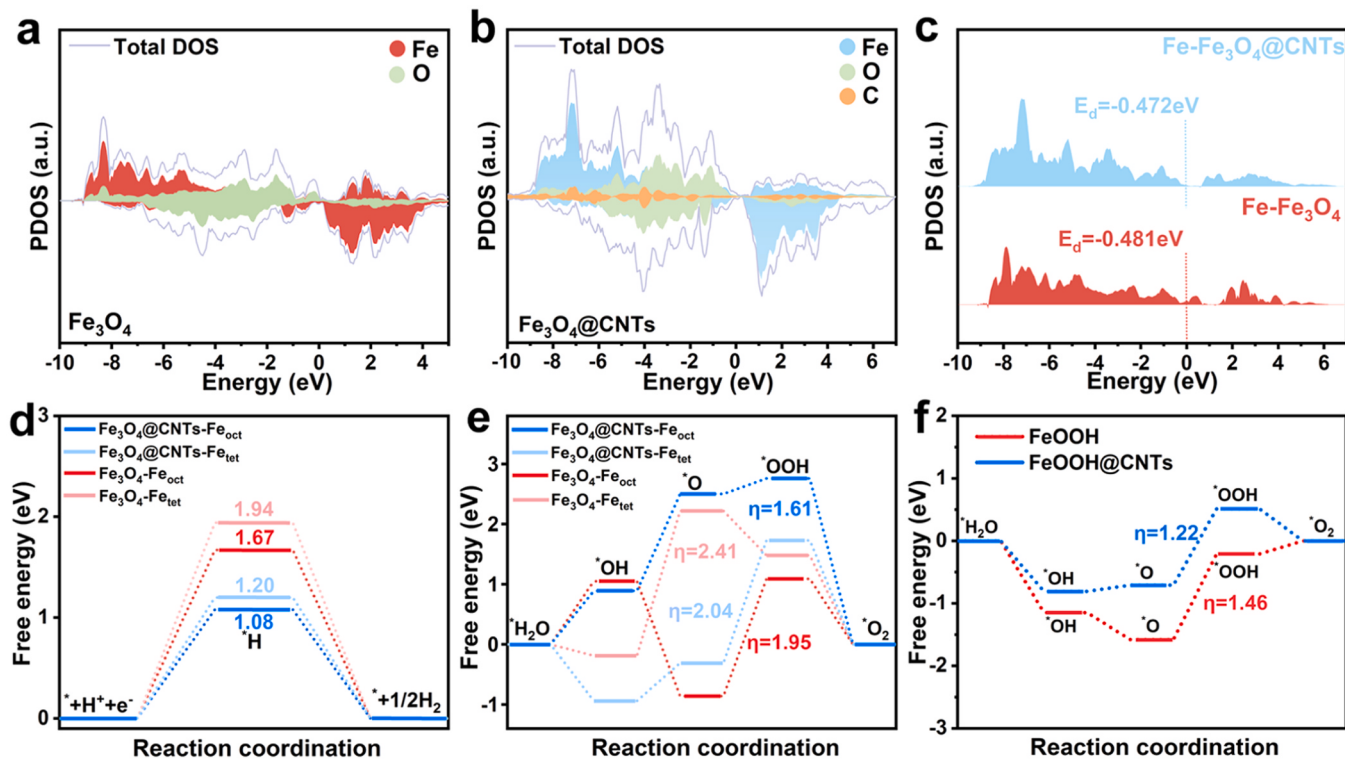


Fig. 2. DOS of (a) Fe_3O_4 and (b) $\text{Fe}_3\text{O}_4@\text{CNTs}$. (c) The d -band centers of Fe 3d in Fe_3O_4 and $\text{Fe}_3\text{O}_4@\text{CNTs}$. Gibbs free energy diagrams of Fe_3O_4 - Fe_{tet} , Fe_3O_4 - Fe_{oct} , $\text{Fe}_3\text{O}_4@\text{CNTs}$ - Fe_{tet} and $\text{Fe}_3\text{O}_4@\text{CNTs}$ - Fe_{oct} for the (d) HER and (e) OER. (f) Gibbs free energy diagrams of FeOOH and $\text{FeOOH}@{\text{CNTs}}$ for the OER.

Fe_3O_4 and $\text{Fe}_3\text{O}_4@\text{CNTs}$ are calculated to be -0.481 and -0.472 eV, respectively, which indicates that the introduction of carbon nanotubes induces the Fe d-band center to move toward the Fermi energy level. Compared to the pure phase, Fe in the heterostructure is less filled on the d-orbitals and has more empty orbitals to receive electrons, resulting in a lower potential barrier to overcome for electron transfer, and thus $\text{Fe}_3\text{O}_4@\text{CNTs}$ can exhibit higher catalytic activity. Notably, $\text{Fe}_3\text{O}_4@\text{CNTs}$ presents a higher state at the energy level close to the Fermi level compared to the pure Fe_3O_4 , which suggests its high electrical conductivity and fast electron transfer capability in the electrocatalytic processes. To further unveil the actual high activity site for hydrogen evolution reaction, we calculated in detail the Gibbs free energy of H^* intermedium state (ΔG_{H^*}) for Fe_3O_4 and $\text{Fe}_3\text{O}_4@\text{CNTs}$ with

Fe_{tet} and Fe_{oct} sites (Figure S4-S7), respectively [30]. As shown in Figure 2d, the $|\Delta G_{\text{H}^*}|$ value of the Fe_{oct} site in the pure Fe_3O_4 is 1.67 eV, which is smaller than that of the Fe_{tet} site (1.94 eV), suggesting that the hexa-coordinated Fe site is more favorable for the HER reaction. For the $\text{Fe}_3\text{O}_4@\text{CNTs}$ heterostructure, the free energies of Fe_{tet} and Fe_{oct} sites are further reduced to 1.08 eV and 1.20 eV, respectively. The above calculations on the free energies of hydrogen precipitation elucidate the contribution of heterostructures to the activity enhancement of the Fe_3O_4 , and importantly, identify the Fe_{oct} in the spinel Fe_3O_4 as the active sites for HER.

There is still considerable controversy over identifying the actual active species of metal oxides during OER reactions under alkaline conditions [31]. The first viewpoint is that metal oxides are considered

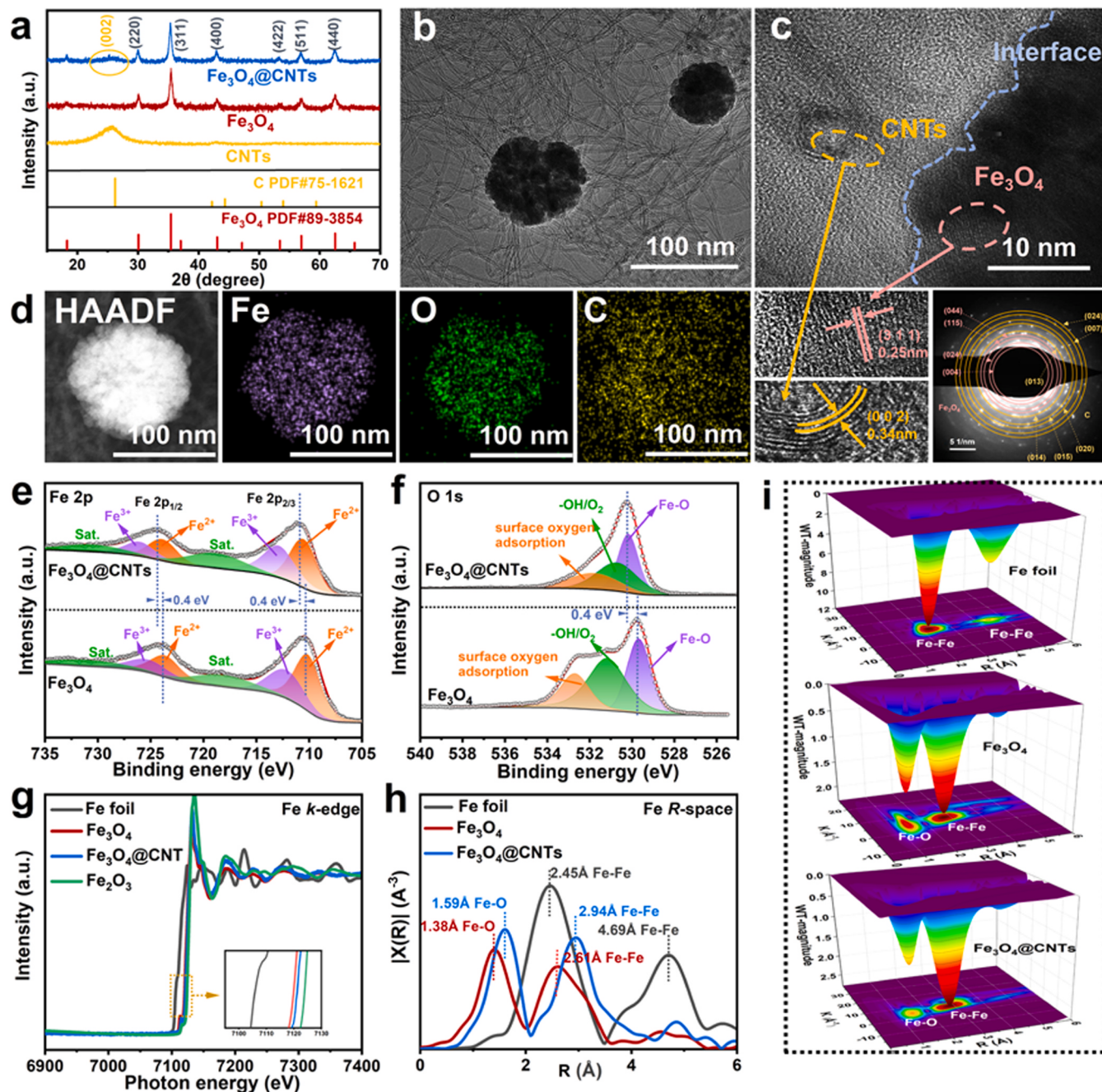


Fig. 3. (a) XRD pattern of Fe_3O_4 , CNTs and $\text{Fe}_3\text{O}_4@\text{CNTs}$. (b) TEM image and (c) HRTEM of $\text{Fe}_3\text{O}_4@\text{CNTs}$. (d) corresponding elements mapping distribution of $\text{Fe}_3\text{O}_4@\text{CNTs}$. (e) XPS Fe 2p and (f) O 1s spectra of Fe_3O_4 and $\text{Fe}_3\text{O}_4@\text{CNTs}$. (g) XANES Fe k -edge spectra and (h) Fourier transform curves of Fe k -edge EXAFS in R-space of Fe_3O_4 , $\text{Fe}_3\text{O}_4@\text{CNTs}$ and Fe foil. (i) Their wavelet transform for k^3 -weighted extended XAFS signals.

as the actual active species in the catalytic process [32]. Another group of researchers categorizes them as "pre-catalysts", in which the electrochemically induced surface reconstruction during catalysis is identified as the active species [33]. Therefore, we further constructed the theoretical calculations for the oxygen evolution reaction on pure FeOOH and FeOOH@CNTs to confirm the active species after surface reconstruction (Figure S8-S9). OER calculations based on the first viewpoint: As shown in Fig. 2d, the proton/electron transfer step with the most significant change in free energy during the endothermic process is the rate-determining step (RDS) that limits the OER [34]. We found that it exhibits the RDS energy barrier of 2.41 eV and 1.95 eV, respectively, indicative of better OER activity of Fe_{oct} compared to Fe_{tet} sites in the spinel Fe₃O₄ (Figure S10-S11). With the introduction of carbon nanotubes, the Fe_{tet} and Fe_{oct} sites in Fe₃O₄@CNTs deliver OER catalytic activity enhancement with an overpotential of 2.04 and 1.61 V, respectively (Figure S12-S13). OER calculations based on the second viewpoint: Figure S14-S15 show the optimized structures of the pure FeOOH and FeOOH@CNTs (010) lattices, respectively. Their corresponding OER reaction pathway on the pure FeOOH and FeOOH@CNTs in Fig. 2f exhibits that their RDS energy barriers are 1.46 eV and 1.22 eV, respectively. The results suggest that introducing carbon tubes can further optimize the OER activity of FeOOH species. According to the above theoretical calculations, the activity of FeOOH is significantly better than that of Fe₃O₄, which aligns with the second viewpoint. Still, this conclusion needs further verification by systematic characterization and electrochemical tests.

Subsequently, we prepare the Fe₃O₄@CNTs catalyst by an extremely simple one-step hydrothermal experimental mean (specific preparation steps are detailed in the [supporting information](#)), and further verify the reliability of the catalytic reaction mechanism derived from the theoretical analyses with the help of systematic characterization and electrochemical tests. X-ray diffraction (XRD) and Raman characterization techniques were utilized to measure the crystal information of the prepared samples [35]. The XRD patterns of the pure Fe₃O₄, CNTs and Fe₃O₄@CNTs samples are displayed in Fig. 3a. All diffraction peaks of the red curve belong to the Fe₃O₄ corresponding to standard PDF#89–3854, while the (002) diffraction peak on the green curve is attributed to carbon (PDF#75–1621), which proves that the two synthesized single-phase substances are Fe₃O₄ and CNTs, respectively [36, 37]. More importantly, all the diffraction characteristic peaks in the sample (Fe₃O₄@CNTs) represented by the blue curve match exactly with the two substances printed above, confirming that it is composed of Fe₃O₄ and CNTs. In addition, Figure S17 shows the XRD patterns of the catalysts synthesized at different Fe-concentrations, which are also composed of Fe₃O₄ and CNTs as can be seen by comparative observation. As shown in Figure S18, the first characteristic peak of the Fe₃O₄@CNTs at 677 cm⁻¹ belongs to Fe₃O₄, while the three characteristic peaks D, G and 2D at 1336, 1577 and 2664 cm⁻¹ correspond well to CNTs [38]. Raman's findings further confirm that the Fe₃O₄@CNTs catalyst contains only Fe₃O₄ and CNTs species, consistent with the XRD analysis above.

Next, the morphology, crystallinity and other essential parameters of the prepared catalysts were obtained using characterization tools such as SEM, specific surface area and hydrophilicity, as described in detail in the [Supporting Information](#) (Figure S19-S27). TEM image is displayed in Fig. 3b, from which we can clearly observe that Fe₃O₄ spheres with a diameter of 100 nm are very uniformly anchored to the carbon nanotubes with a diameter of about 5 nm. As shown in Fig. 3c, the spacing of the lattice stripes at the green-marked portion is 0.34 nm corresponding to the (002) face of CNTs; the red-marked portion with a face spacing of 0.25 nm corresponds to the (311) face of Fe₃O₄. It is extremely exciting that the interface where Fe₃O₄ and CNTs are in close contact can be clearly observed in the HRTEM image. Meanwhile, its mapping diagram also confirms that the sample is made of nanospheres composed of Fe₃O₄ interconnected with CNTs (Fig. 3d). X-ray photoelectron spectroscopy (XPS) analyzed the changes in the surface elemental states and

electronic structures of Fe₃O₄ before and after the construction of the heterostructure. Among them, their XPS survey and C 1 s spectrum are presented in Figure S28 and S29. The high-resolution Fe 2p spectra of Fe₃O₄ and Fe₃O₄@CNTs comprise of Fe²⁺ peaks, Fe³⁺ peaks and two additional satellite peaks. For Fe₃O₄, these characteristic peaks are located at 710.2, 712.5, 723.9, and 725.8 eV, corresponding to Fe²⁺ 2p_{3/2}, Fe³⁺ 2p_{3/2}, Fe²⁺ 2p_{1/2}, and Fe³⁺ 2p_{1/2}, respectively [39]. It is clearly observed from Fig. 3e that the characteristic peaks of both the Fe²⁺ and Fe³⁺ species in Fe₃O₄@CNTs are shifted to higher binding energies by about 0.4 eV compared to the Fe 2p state in Fe₃O₄, suggesting that Fe₃O₄ acts as an electron donor for charge transfer to the CNTs [40]. Fig. 3f displays that their high-resolution spectrum of O 1 s can be divided into three peaks at 529.6, 531.1, and 532.7 eV, corresponding to lattice oxygen (Fe-O), adsorbed oxygen (OH/O₂) and surface adsorbed oxygen, respectively [41]. It is worth mentioning that compared with Fe₃O₄, lattice oxygen peaks shift to a higher binding energy in the Fe₃O₄@CNTs, suggesting that the introduction of CNTs leads to electron deficiency in lattice oxygen. Meanwhile, the charge density difference calculations (Figure S30) further indicate that the charge is transferred from lattice oxygen to CNTs, after contact with the Fe₃O₄ surface.

The Fe K-edge X-ray absorption near edge structure spectra (XANES) of pure Fe₃O₄, Fe₃O₄@CNTs and Fe foil catalysts are displayed in Fig. 3g. The edge peak of Fe₃O₄@CNTs has a slightly positive shift and higher white line intensity compared to that of pure Fe₃O₄, which suggests that the interfacial effect between Fe₃O₄ and CNT in the heterostructure exacerbates the further electron precipitation from the Fe sites, i.e., an elevated Fe valence state [42,43]. In addition, the EXAFS oscillations of the k³-weighted data (Figure S31) show that Fe₃O₄@CNTs produces a smaller amplitude and an increase in the coordination number of Fe sites, which also suggests an elevated Fe valence state, which is in full agreement with the elevated Fe³⁺/Fe²⁺ molar ratio in XPS results [44]. As shown in Fig. 3h, the main peaks of the pure Fe₃O₄ at about 1.38 and 2.61 Å attributed to Fe-O and Fe-Fe bonds, respectively. Compared to the pure phase, the length of the Fe-O bond in the Fe₃O₄@CNTs shifts towards a higher radial distance of 2.94 Å, which proves a distortion of the internal structure, thus confirming the existence of a partial bonding between the Fe₃O₄ and CNTs, rather than a non-bonding van der Waals composite (Fig. 3i) [45].

On the above theoretical analysis and experimental characterization, we next need to evaluate its catalytic performance and mechanism more intuitively by electrochemical testing means and *in-situ* characterization techniques. In [supporting information](#), comparisons of HER and OER for the samples prepared at different Fe-concentrations are detailed in Figure S32 and Figure S33. Fig. 4a and Figure S34 illustrate the linear sweep voltammetry (LSV) curves for HER and the corresponding Tafel slope of Fe₃O₄@CNTs, pure Fe₃O₄, Ni foam, CNTs and Pt/C, respectively. Their LSV curves show that the optimal Fe₃O₄@CNTs catalyst requires only 89 mV to achieve a current density of 10 mA cm⁻², which is significantly better than that of pure Fe₃O₄ (128 mV) nanoparticles and CNTs (107 mV). Figure S34 shows that Fe₃O₄@CNTs converts to a Tafel slope of 117 mV dec⁻¹, which is also superior to those of Fe₃O₄ (149 mV dec⁻¹) and CNTs (170 mV dec⁻¹), demonstrating excellent catalytic activity and reaction kinetics. In addition to studying the catalytic activity of the catalyst, its stability over a long period of time plays a crucial role in practical applications [46]. As shown in Fig. 4b, at a high current density of 100 mA cm⁻², the activity retention of Fe₃O₄@CNTs can still reach more than 94.8% after 500 hours of stable operation. As shown in Figure S35, the XRD and Raman pattern of the Fe₃O₄@CNTs after cycling remain in perfect agreement with their initial states, and there is no change in the microstructure before and after the reaction (Figure S36), indicating excellent electrochemical stability.

In the field of OER performance, Fig. 4c shows the LSV of the Fe₃O₄@CNTs, pure Fe₃O₄, CNTs, Ni foam and RuO₂. Pure Fe₃O₄ presents an absolute advantage in OER performance as it requires only 318 mV to reach a current density of 100 mA cm⁻², whereas RuO₂,

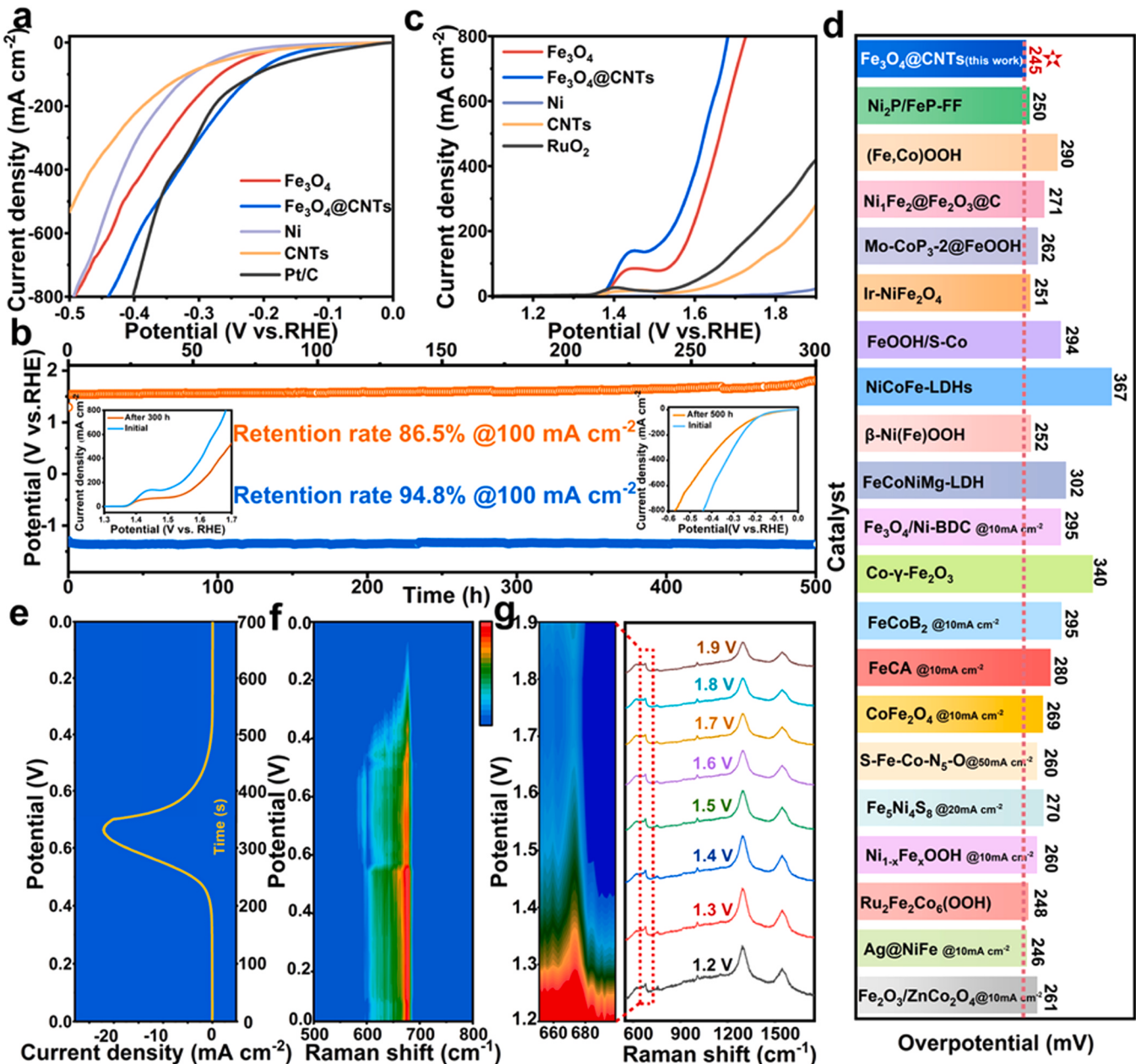


Fig. 4. (a) HER linear sweep voltammetry curves of $\text{Fe}_3\text{O}_4@\text{CNTs}$, Fe_3O_4 , Ni foam, CNTs and commercial Pt/C in 1.0 M KOH solution. (b) Long-time chronoamperometric curve of $\text{Fe}_3\text{O}_4@\text{CNTs}$ for HER and OER (inset: LSV for initial and after activity reaction). (c) OER linear sweep voltammetry curves of $\text{Fe}_3\text{O}_4@\text{CNTs}$, Fe_3O_4 , Ni foam, CNTs and RuO_2 in 1.0 M KOH solution. (d) Comparison of OER activities for $\text{Fe}_3\text{O}_4@\text{CNTs}$ with recently reported Fe-based catalysts [17,39,S4–21]. (e) The evolution of the initial CV cycle in the potential range of 0–0.7 V at a scan rate of 1 mV s^{-1} . (f) Operando Raman spectra of $\text{Fe}_3\text{O}_4@\text{CNTs}$ during the initial CV cycle. (g) *in-situ* Raman spectra of $\text{Fe}_3\text{O}_4@\text{CNTs}$ tested at different potentials (vs. RHE).

CNTs and Ni foams require 360 mV, 512 mV and 690 mV, respectively. Surprisingly, the $\text{Fe}_3\text{O}_4@\text{CNTs}$ catalyst exhibits enhanced OER catalytic activity (243 mV at 100 mA cm^{-2}), which surpassed most of the reported transition metal compound-based catalysts (Fig. 4d). Similarly, the corresponding Tafel slopes for samples such as $\text{Fe}_3\text{O}_4@\text{CNTs}$ and RuO_2 are shown one by one in Figure S37. So OER activity also positively reflects the superiority of constructing $\text{Fe}_3\text{O}_4@\text{CNTs}$ heterostructures. From an industrial application point of view, the durability testing of catalysts at high current densities is a critical technical factor to assess their commercialization value. As shown in Fig. 4b, the activity loss rate of $\text{Fe}_3\text{O}_4@\text{CNTs}$ is about 13.5% after more than 300 h of stable OER operation at a high current density of constant 100 mA cm^{-2} . Figure S38 shows no significant change in the morphology of the $\text{Fe}_3\text{O}_4@\text{CNTs}$ before and after the oxygen revolution reaction. However,

peaks belonging to hydroxyl hydroxides (PDF#81–0464) can be found in the XRD patterns of the post-reaction samples (Figure S39), which indicates the generation of FeOOH during the OER reaction[41]. As shown in Figure S40, the Raman spectra before and after the OER show the attenuated Fe-O vibrational modes due to the generation of amorphous FeOOH during the reaction, consistent with the XRD characterization [47]. Furthermore, we can observe a thin amorphous FeOOH shell layer in the outermost layer of the Fe_3O_4 spheres from the TEM images after OER, which directly confirms the existence of the surface remodeling process after the reaction (Figure S41).

The theoretical calculation results indicate that FeOOH is more favorable than Fe_3O_4 for OER-catalyzed reactions (Fig. 2f). The electrochemical reconstruction phenomenon during the reaction was further investigated by cyclic voltammetry, chronopotentiometry tests and *in-*

situ Raman to clarify the actual active species during the OER process [27]. Theoretically, the release and accumulation of oxygen during the OER process increase the internal concentration of oxygen intermediates, leading to Fe_3O_4 corrosion and the formation of FeOOH [48]. Therefore, cyclic voltammetry curves with the applied potential (0–0.6 V) and chronopotentiometry curves measured at a constant current density of 1 mA cm^{-2} are used to observe their reconstruction phenomenon. As shown in Figure S42a, the obvious Fe redox peaks in the CV curves of both the pure Fe_3O_4 and $\text{Fe}_3\text{O}_4@\text{CNTs}$ represent the material's reconstruction process and the production of new species

[49]. As seen from Figure S42b, the curve over time rises from the initial potential up to about 1.5 V. Then it remains constant, corresponding to the gradual generation of $\text{Fe}-\text{OOH}$ on the catalyst surface [49].

Furthermore, we employ advanced operando Raman spectroscopy to study the dynamics of the surface reconstruction during the real-time catalytic process. Fig. 4e depicts the CV test of a time-current-voltage relationship for an applied voltage of 0–0.7 V under actual OER conditions. Fig. 4f and Figure S42 show that its dynamic reconstruction process can be divided into the surface stationary phase from 0 to 0.4 V (0–200 s) and the surface reconstruction phase from 0.4 to 0.7 V and

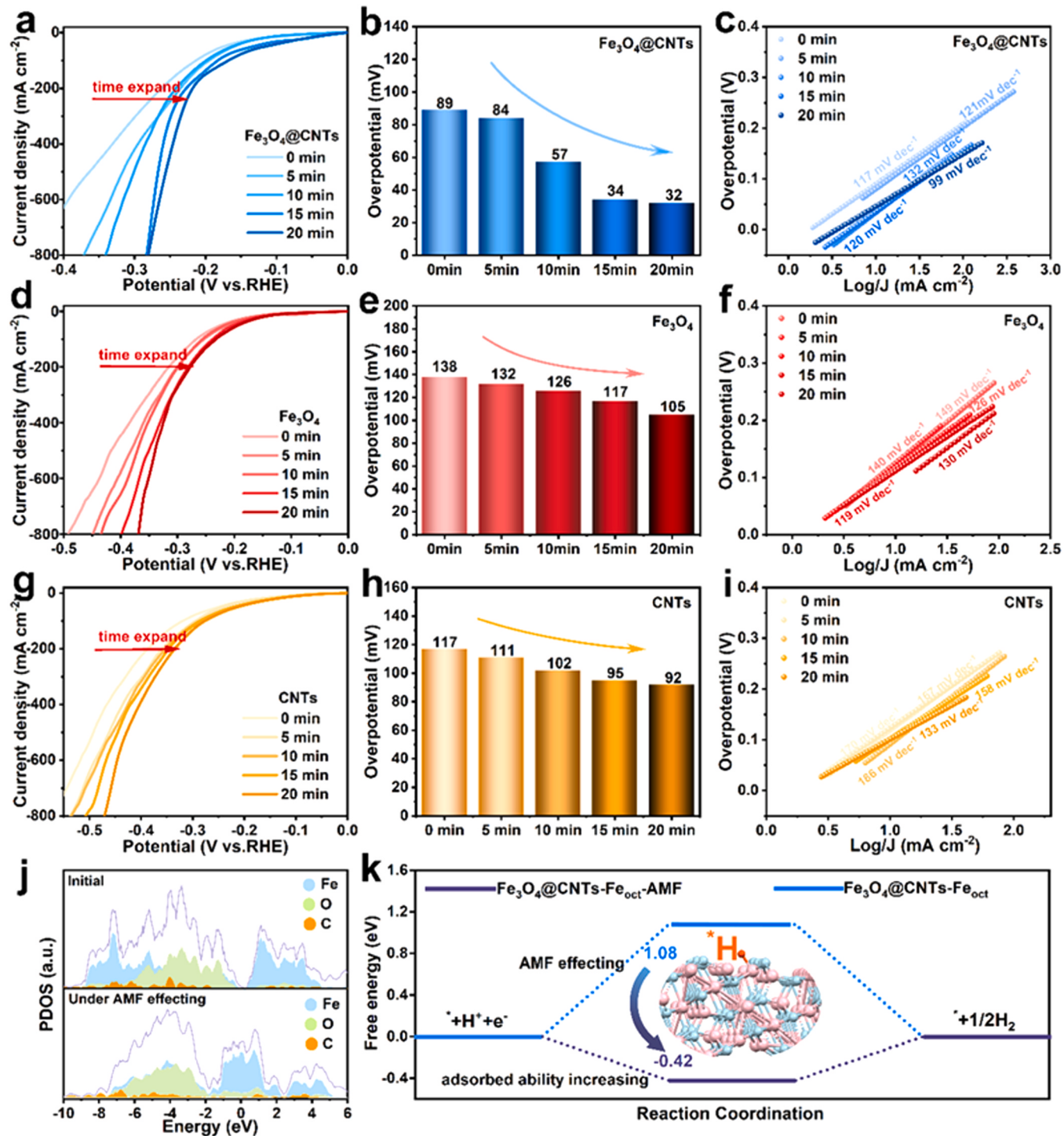


Fig. 5. HER linear sweep voltammetry curves under AMF impacting, corresponding overpotentials at 10 mA cm^{-2} current density and Tafel slopes of (a-c) $\text{Fe}_3\text{O}_4@\text{CNTs}$, (d-f) Fe_3O_4 and (g-i) CNTs. (j) DOS of $\text{Fe}_3\text{O}_4@\text{CNTs}$ with and without AMF effecting. (k) Gibbs energy diagrams for the HER with or without AMF.

0.7–0 V (200–700 s). The intensity of the Raman peak at 677 cm⁻¹ belonging to the Fe-O vibration remains unchanged, indicating that the Fe₃O₄@CNTs catalyst does not undergo a phase transition during the surface stationary phase. For its surface reconstruction phase, the intensity of the Raman peak at 677 cm⁻¹ decreases with the increase of time, which demonstrates the gradual conversion of Fe₃O₄ species to amorphous FeOOH. In addition, by observing and comparing the *in-situ* Raman spectra tested at different potentials, we also find that the intensity of Fe-O vibration tends to diminish with increasing potential, which indicates the production of FeOOH species after surface reconstruction during the OER process (Fig. 4g) [50].

Although the construction of heterostructures has played a significant effect on the intrinsic activity enhancement of the materials, as far as the present study results are concerned, especially for HER, its activity is still lower than that of noble metal Pt/C catalyst (43 mV of overpotential at 10 mA cm⁻²). Therefore, it is apparent that relying only on material modification to improve its performance is insufficient. Then, how to further enhance its activity is a great challenge we are currently facing. An external magnetic field can force the moving carriers in magnetic materials [51], which leads to changes in the charge transport inside the materials and turns the adsorption interaction between adsorbates and substrates [52]. To this purpose, we propose a novel AMF modulation strategy in the hope of further improving the charge directional transport rate in heterogeneous structures and the mass transfer effect on catalytic surfaces by introducing an external alternating magnetic field, thus realizing a big leap in electrocatalytic activity.

A schematic diagram of the experimental setup for electrocatalysis under an alternating magnetic field is shown in Figure S48. Fig. 5a-c displays the variations of HER linear sweep voltammetry curves, overpotentials and corresponding Tafel slope of the optimal Fe₃O₄@CNTs, pure Fe₃O₄ and CNTs in an alternating magnetic field. As displayed in Fig. 5a and 5b, the overpotentials of Fe₃O₄@CNTs at a current density of 10 mA cm⁻² are 89, 84, 57, 34, and 32 mV after 5, 10, 15, and 20 min of alternating magnetic field, respectively. Landmarkly, its activity under the synergistic modulation of alternating magnetic field far exceeds that of the commercial Pt/C. Under the same test conditions, the overpotentials of pure Fe₃O₄ (Fig. 5d, e) and CNTs (Fig. 5g, h) at 10 mA cm⁻² are 138, 132, 126, 117, 105 mV and 117, 111, 102, 95, 92 mV, respectively. From the above test results, the HER activity of all three samples shows an increasing trend with time and peaks after 20 minutes. Meanwhile, their corresponding Tafel slopes gradually decrease with the decrease of overpotentials: the optimal Fe₃O₄@CNTs descends from 117 to 99 mV dec⁻¹ (Fig. 5c), pure Fe₃O₄ from 149 to 130 mV dec⁻¹ (Fig. 5f) and CNTs from 177 to 133 mV dec⁻¹ (Fig. 5i), suggesting that the kinetics of their catalytic reactions are similarly optimized. All samples prepared at different Fe-concentrations were tested under the same experimental conditions to determine that this activity change under an alternating magnetic field is not an occasional phenomenon. As shown in Figure S49-51, the electrochemical testing results of those samples exhibit the same trend as mentioned above, which confirms the positive effect of the alternating magnetic field on HER catalytic activity.

As shown in Figure S52, the magnetic hysteresis loop results show that both the pure Fe₃O₄ and the Fe₃O₄@CNTs display soft magnetic properties, with saturation magnetizations of 63.84 and 58.77 emu g⁻¹, respectively. After comparison, it can be clearly found that the magnetization strength of the pure phase is greater than that of the heterogeneous structure, so theoretically the effect of the alternating magnetic field on the pure phase should be greater than that of the heterogeneous structure. However, the result is that the enhancement of the Fe₃O₄@CNTs heterogeneous catalyst is higher than that of the pure Fe₃O₄, indicating that the alternating magnetic field can effectively accelerate the directional transfer of charge inside the heterogeneous structure. To gain a deeper understanding of the mechanism by which the magnetic field improves the catalytic activity of the Fe₃O₄@CNTs, we analyzed the changes in its free energy before and after the

application of the magnetic field using the constrained local magnetic moments DFT calculations. To clearly compare the orbital interactions in low/high-spin state Fe-3d and O-2p, the DOS results of Fe₃O₄@CNTs with and without AMF effecting were shown in the Fig. 5j. The results show that the initial Fe₃O₄@CNTs sample has the Fe-3d orbitals at the energy range of -0.5 to -9 eV, and O-2p orbitals at the -0.5 to -7 eV. At the energy range of -6 to -9 eV, the sample shows less overlap between the Fe-3d and O-2p states. After adding the AMF effect to the sample, Fe-3d orbitals shift to a higher energy level. At the energy range of -2 to -7 eV, there is increased overlap between the Fe-3d and O-2p states, indicating enhanced hybridization of 3d-2p orbitals in the Fe₃O₄@CNTs heterogeneous catalyst. This enhanced hybridization leads to the activation of the Fe_{oct} sites and significantly promotes charge transfer between the slab and intermediates [52]. Furthermore, the activated high-spin state of Fe_{oct} can facilitate the HER kinetics due to the improved $\sigma^*/\sigma(d_z^2, s)$ interaction. As illustrated in Fig. 5k, it is evident that the Gibbs free energy of the H* intermediate state in the presence of a magnetic field is more closely aligned with the ideal value of 0 eV, as compared to the Fe₃O₄@CNTs without a magnetic field. These results pave a new way to break the hydrogen evolution activity bottleneck in the design modifications of catalysts.

Encouraged by the fact that the alternating magnetic field enhances the HER activity of the catalyst, we continue to explore its effect on the OER. Fig. 6a-c displays the variations of OER electrocatalytic activities under the effect of an alternating magnetic field. Similarly, as the alternating magnetic field duration is increased to 20 minutes, the overpotential of Fe₃O₄@CNTs catalyst decreases by 66 mV from the original 245 mV, which means that only 179 mV is needed to reach a current density of 100 mA cm⁻² (Fig. 6a and 6b). As interesting as all this is, the overpotential to reach 100 mA cm⁻² for pure Fe₃O₄ (Fig. 6d, e) and CNTs (Fig. 6g, h) decrease from 318 mV to 259 mV and 512 mV to 479 mV, respectively, which is a reduction of 59 mV and 33 mV, respectively, compared to the original data. From Fig. 6a and 6d, a discernible trend becomes apparent in the observation that the occurrence of the generated oxidation peak (FeOOH species) gradually advances as the duration of the applied magnetic field increases. To elucidate the underlying mechanism responsible for such acceleration, carry out the formation energy calculations of FeOOH under non-spin and high-spin states based on the equation ($E_f(FeOOH)=E_{(FeOOH)}-\chi\mu_{(Fe)}-yE_O-z\mu_{(Fe)}$). The results indicate that FeOOH exhibits a lower formation energy of -62.596 eV in a high spin state compared to -35.796 eV in a non-spin state, which reveals that the magnetic field can accelerate the reconstruction of Fe₃O₄ into FeOOH (Table S4). This phenomenon strongly implies that the introduction of the magnetic field prompts an earlier initiation of surface reconstruction in Fe₃O₄, subsequently expediting the catalytic reaction rate. For OER reaction kinetics, the Tafel slope corresponding to Fe₃O₄@CNTs decreases from 210 mV dec⁻¹ to 91 mV dec⁻¹ (Fig. 6c). To explore the generalization of an alternating magnetic field to the materials, the OER activity of samples prepared at different Fe-concentrations was also tested. As shown in Figure S53-55, the OER activities of the samples are all increased to some extent under the influence of the alternating magnetic field.

To elucidate the magnetic field-induced enhancement mechanism on the OER reaction of Fe₃O₄@CNTs, we analyzed the change in its free energy before and after the application of the magnetic field with the help of DFT calculations. Based on the dependence between the OER activity and the free energy of the reaction intermediates, we evaluate the change of Gibbs free energy in each reaction step of FeOOH@CNTs under the influence of the magnetic field. The OER predominantly hinges on the interplay of multi-orbital hybridizations: 1. The d, p hybridization system, comprising the d_z^2 , d_{xz} , and d_{yz} orbitals interacting with the 2p orbitals of oxygen atoms. 2. The d, p, s hybridization system, involving the d_z^2 , d_{xz} , and d_{yz} orbitals with OH* and OOH* oxygen-containing intermediates. The introduction of a magnetic field enhances the orbital overlap between the d and p orbitals, refining the bonding interactions. As shown in Fig. 6j, the energy barrier of

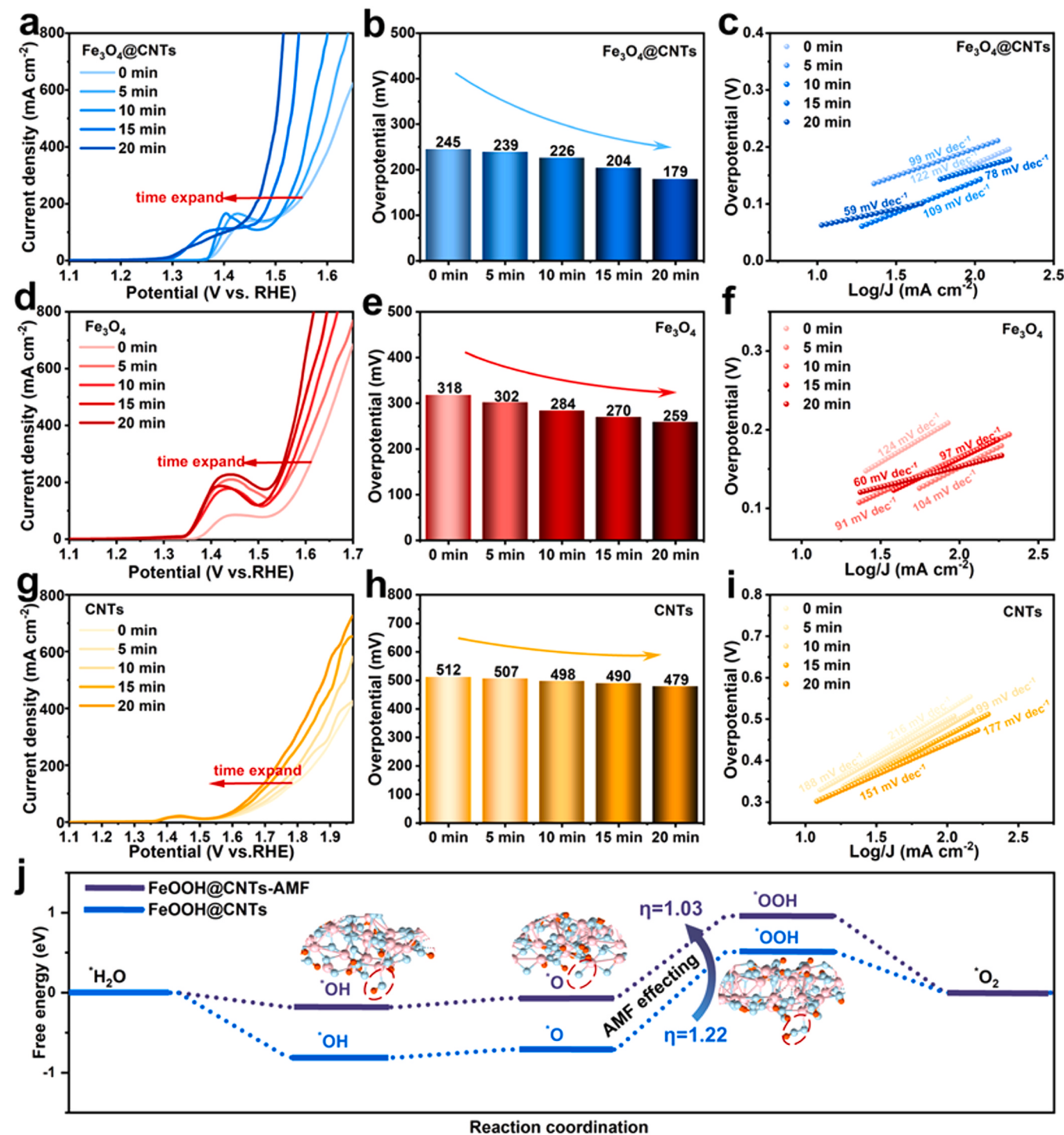


Fig. 6. OER linear sweep voltammetry curves under AMF impacting, corresponding overpotentials at 100 mA cm⁻² current density and Tafel slopes of (a-c) Fe₃O₄@CNTs, (d-f) Fe₃O₄ and (g-i) CNTs. (j) Gibbs energy diagrams for OER with or without AMF.

FeOOH@CNTs is reduced from 1.22 eV in the initial state to 1.03 eV under the magnetic field, which demonstrates that the magnetic field could further optimize the adsorption-desorption capacity to improve its OER catalytic activity. For the OER, the magnetic field not only accelerates the generation of active species, but also enhances the adsorption-desorption rate of oxygen-containing intermediates on the surface of the catalyst, thus confirming the positive effect of the magnetic field on the OER performance.

4. Conclusion

In summary, with the help of DFT calculations, *in-situ* Raman and XAS characterization, we have elucidated in detail that the optimal active site for spinel Fe₃O₄-based catalysts is hexa-coordinated Fe sites for HER. In contrast, the active species for OER is the FeOOH species generated by surface reconstruction. In order to break through the bottleneck of material modification to enhance the catalytic activity, we innovatively proposed a magnetron regulation strategy. The alternating magnetic field excites the high spin configurations of the Fe_{oct} sites and

facilitates the multiple orbital interactions of $\sigma(d_z^2, p_z, s)$ and $\pi(d_{xz}, p_x, d_{yz}, p_y)$ between intermediates and active sites. The unpaired d electrons yield accelerated charge transfer and optimized adsorption and desorption interactions to intermediates in the reaction processes, thereby significantly enhancing the electrocatalytic activity. For HER, the magnetic field also improves the ability of H^* intermedium adsorption and desorption, thus increasing the catalytic reaction efficiency. In the case of another half-reaction, the magnetic field not only accelerates the generation of FeOOH active species, but also enhances the adsorption-desorption rate of oxygen-containing intermediates on the surface of the catalyst, thus confirming the positive effect of the magnetic field on the OER performance. This work provides a new way of thinking to break through the bottleneck of nanomaterials performance enhancement.

CRediT authorship contribution statement

Haiqin Zhang: Software, Investigation. **Xiyue Li:** Software, Investigation. **Liguang Lin:** Validation, Investigation, Data curation. **Yixue Zhang:** Validation, Funding acquisition. **Jianbo Sun:** Software. **Xinyuan Wang:** Investigation. **Hongyao Xue:** Writing – review & editing, Writing – original draft, Project administration, Investigation, Funding acquisition, Formal analysis, Data curation, Conceptualization. **Jiacheng Wang:** Software, Methodology, Investigation, Formal analysis, Data curation, Conceptualization. **Xiaobin Liao:** Methodology, Investigation, Conceptualization. **Yan He:** Visualization, Validation, Supervision, Resources, Project administration, Funding acquisition. **He Cheng:** Software, Methodology, Investigation, Formal analysis, Data curation.

Declaration of Competing Interest

The authors declare that they have no known competing financial interests or personal relationships that could have appeared to influence the work reported in this paper.

Data Availability

No data was used for the research described in the article.

Acknowledgments

The authors gratefully acknowledge financial support from the National Natural Science Foundation of China (No. 52302098, 52336003, 52176076, 51676103), China Postdoctoral Science Foundation (2023M731855), Taishan Scholar Project of Shandong Province (China) (No. ts20190937), Natural Science Foundation of Shandong Province (China) (No. ZR2023QE344, ZR2021LFG003) and Qingdao Postdoctoral Science Foundation (No. QDBSH20220201021, QDBSH20220202084). We would like to thank Zhang Jing from Shidianjia Lab (www.shidianjia.com) for the XPS analysis.

Appendix A. Supporting information

Supplementary data associated with this article can be found in the online version at [doi:10.1016/j.apcatb.2024.124087](https://doi.org/10.1016/j.apcatb.2024.124087).

References

- [1] X. Hai, Y. Zheng, Q. Yu, N. Guo, S.B. Xi, X.X. Zhao, S. Mitchell, X.H. Luo, V. Tulus, M. Wang, X.Y. Sheng, L.B. Ren, X.D. Long, J. Li, P. He, H.H. Lin, Y.G. Cui, X. N. Peng, J.W. Shi, J. Wu, C. Zhang, R.Q. Zou, G. Guillen-Gosalbez, J. Perez-Ramirez, M.J. Koh, Y. Zhu, J. Li, J. Lu, Geminal-atom catalysis for cross-coupling, *Nature* 622 (2023) 754–760.
- [2] L.N. Chong, G.P. Gao, J.G. Wen, H.X. Li, H.P. Xu, Z. Green, J.D. Sugar, A.J. Kropf, W.Q. Xu, X.M. Lin, H. Xu, L.W. Wang, D.J. Liu, La- and Mn-doped cobalt spinel oxygen evolution catalyst for proton exchange membrane electrolysis, *Science* 380 (2023) 609–616.
- [3] M.Z. You, X. Du, X.H. Hou, Z.Y. Wang, Y. Zhou, H.P. Ji, L.Y. Zhang, Z.T. Zhang, S. S. Yi, D.L. Chen, In-situ growth of ruthenium-based nanostructure on carbon cloth for superior electrocatalytic activity towards HER and OER, *Appl. Catal. B Environ.* Energy 317 (2022) 121729.
- [4] A. Saad, D.Q. Liu, Y.C. Wu, Z.Q. Song, Y. Li, T. Najam, K. Zong, P. Tsakaras, X. K. Cai, Ag nanoparticles modified crumpled borophene supported Co_3O_4 catalyst showing superior oxygen evolution reaction (OER) performance, *Appl. Catal. B Environ.* Energy 298 (2021) 120529.
- [5] J. Wu, X. Wang, W.H. Zheng, Y. Sun, Y. Xie, K.K. Ma, Z. Zhang, Q.L. Liao, Z. Tian, Z. Kang, Y. Zhang, Identifying and interpreting geometric configuration-dependent activity of spinel catalysts for water reduction, *J. Am. Chem. Soc.* 144 (2022) 19163–19172.
- [6] E. Bianchetti, D. Perilli, C.D. Valentini, Improving the oxygen evolution reaction on $Fe_3O_4(001)$ with single-atom catalysts, *ACS Catal.* 13 (2023) 4811–4823.
- [7] K. Li, R.R. Zhang, R.J. Gao, G.Q. Shen, L. Pan, Y.D. Yao, K.H. Yu, X.W. Zhang, J. J. Zou, Metal-defected spinel $MnxCo_{3-x}O_4$ with octahedral Mn-enriched surface for highly efficient oxygen reduction reaction, *Appl. Catal. B Environ.* Energy 244 (2019) 536–545.
- [8] Y. Wang, M.M. Wu, K. Wang, J.W. Chen, T.W. Yu, S.Q. Song, Fe_3O_4 @N-doped interconnected hierarchical porous carbon and its 3D integrated electrode for oxygen reduction in acidic media, *Adv. Sci.* 7 (2020) 2000407.
- [9] S.C. Sun, H. Jiang, Z.Y. Chen, Q. Chen, M.Y. Ma, L. Zhen, B. Song, C.Y. Xu, Bifunctional WC-supported RuO_2 nanoparticles for robust water splitting in acidic media, *Angew. Chem. Int. Ed.* 61 (2022) e202202519.
- [10] R.H. Gan, Y. Song, C. Ma, J.L. Shi, In situ growth of N-doped carbon nanotubes in $Fe-N_x/Fe_2O_3/Fe_3O_4$ -encapsulated carbon sheets for efficient bifunctional oxygen catalysis, *Appl. Catal. B Environ.* Energy 327 (2023) 122443.
- [11] Z.Z. Sun, A. Curto, J. Rodriguez-Fernandez, Z.G. Wang, A. Parikh, J. Fester, M. D. Dong, A. Vojvodic, J.V. Lauritsen, The effect of Fe dopant location in $Co(Fe)OOH_x$ nanoparticles for the oxygen evolution reaction, *ACS Nano* 15 (2021) 18226–18236.
- [12] L. Ran, Y. Xu, X.W. Zhu, S.Y. Chen, X.Q. Qiu, Mn single-atom tuning Fe-N-C catalyst enables highly efficient and durable oxygen electrocatalysis and zinc-air batteries, *ACS Nano* 18 (2024) 750–760.
- [13] X. Chen, M. Yu, Z.H. Yan, W.Y. Guo, G.L. Fan, Y.X. Ni, J.D. Liu, W. Zhang, W. Xie, F.Y. Cheng, J. Chen, Boosting electrocatalytic oxygen evolution by cation defect modulation via electrochemical etching, *CCS Chem.* 2 (2020) 675–685.
- [14] X. Dong, X. Duan, Z. Sun, X. Zhang, C. Li, S. Yang, B. Ren, S. Zheng, D.D. Dionysiou, Natural illite-based ultrafine cobalt oxide with abundant oxygen-vacancies for highly efficient Fenton-like catalysis, *Appl. Catal. B Environ.* Energy 261 (2020) 118214.
- [15] C. Neither, S. Faure, A. Bordet, J. Desure, M. Chatenet, J. Carrey, B. Chaudret, A. Pouet, Improved water electrolysis using magnetic heating of $FeC-Ni$ core-shell nanoparticles, *Nat. Energy* 3 (2018) 476–483.
- [16] F.A. Garces-Pineda, M. Blasco-Ahicart, D. Nieto-Castro, N. Lopez, J.R. Galan-Mascaros, Direct magnetic enhancement of electrocatalytic water oxidation in alkaline media, *Nat. Energy* 4 (2019) 519–525.
- [17] X.G. Gong, Z.Z. Jiang, W. Zeng, C. Hu, X.F. Luo, W. Lei, C.L. Yuan, Alternating magnetic field induced magnetic heating in ferromagnetic cobalt single-atom catalysts for efficient oxygen evolution reaction, *Nano Lett.* 22 (2022) 9411–9417.
- [18] L. Cai, J.T. Huo, P. Zou, G.W. Li, J. Liu, W. Xu, M. Gao, S.Z. Zhang, J.Q. Wang, Key role of lorentz excitation in the electromagnetic-enhanced hydrogen evolution reaction, *ACS Appl. Mater. Interfaces* 14 (2022) 15243–15249.
- [19] G. Zhou, P.F. Wang, H. Li, B. Hu, Y. Sun, R. Huang, L.Z. Liu, Spin-state reconfiguration induced by alternating magnetic field for efficient oxygen evolution reaction, *Nat. Commun.* 12 (2021) 4827.
- [20] X.Z. Liu, P. Zou, L.J. Song, B.W. Zang, B.N. Yao, W. Xu, F.S. Li, J. Schröers, J. T. Huo, J.Q. Wang, Combinatorial high-throughput methods for designing hydrogen evolution reaction catalysts, *ACS Catal.* 12 (2022) 3789–3796.
- [21] D.Q. Peng, C. Hu, X.F. Luo, J.L. Huang, Y. Ding, W.D. Zhou, H. Zhou, Y. Yang, T. Yu, W. Lei, C.L. Yuan, Electrochemical reconstruction of $NiFe/NiFeOOH$ superparamagnetic core/catalytic shell heterostructure for magnetic heating enhancement of oxygen evolution reaction, *Small* 19 (2023) 2205665.
- [22] W. Zeng, W. Jiang, Z.Z. Gong, X.G. Hu, C. Luo, X.F. Lei, W. Yuan, C.L. Yuan, Atomic magnetic heating effect enhanced hydrogen evolution reaction of $Gd@MoS_2$ single-atom catalysts, *Small* 19 (2023) 2206155.
- [23] G. Kresse, J. Furthmüller, Efficient iterative schemes for ab initio total-energy calculations using a plane-wave basis set, *Phys. Rev. B* 54 (1996) 1116.
- [24] J.P. Perdew, K. Burke, M. Ernzerhof, Generalized gradient approximation made simple, *Phys. Rev. Lett.* 77 (1977) 3865.
- [25] S. Grimme, J. Antony, S. Ehrlich, H. Krieg, A consistent and accurate ab initio parametrization of density functional dispersion correction (DFT-D) for the 94 elements H-Pu, *J. Chem. Phys.* 132 (2010) 154104.
- [26] W. Qiao, S.M. Yan, D.Y. Jin, X.Y. Xu, W.B. Mi, D.H. Wang, Vertical-orbital band center as an activity descriptor for hydrogen evolution reaction on single-atom-anchored 2D catalysts, *J. Phys. Condens. Matter* 33 (2021) 245201.
- [27] C. Hu, K.H. Yue, J.J. Han, X.Z. Liu, L.J. Liu, Q.N. Liu, Q.Y. Kong, C.W. Pao, Z. W. Hu, K. Suenaga, D. Su, Q.B. Zhang, X.Y. Wang, Y.Z. Tan, X.Q. Huang, Misoriented high-entropy iridium ruthenium oxide for acidic water splitting, *Sci. Adv.* 9 (2023) ead9f144.
- [28] S. Zhao, F. Hu, L.J. Yin, L.L. Li, S.J. Peng, Manipulating electron redistribution induced by asymmetric coordination for electrocatalytic water oxidation at a high current density, *Sci. Bull.* 68 (2023) 1389–1398.
- [29] Z.F. Huang, J.J. Song, Y.H. Du, S.B. Xi, S. Dou, J.M.V. Nsanzimana, C. Wang, Z.C. J. Xu, X. Wang, Chemical and structural origin of lattice oxygen oxidation in Co-Zn oxyhydroxide oxygen evolution electrocatalysts, *Nat. Energy* 4 (2019) 329–338.

- [30] G.Z. Qin, Y.N. Zhang, J.F. Zheng, Y.F. Li, X.J. Han, Z.G. Huang, Reaction mechanism of selective catalytic reduction of NO with NH₃ on Fe₃O₄ (111) surface: experimental and DFT studies, *Fuel* 349 (2023) 128621.
- [31] Y.M. Sun, J.R. Wang, S.B. Xi, J.J. Shen, S.Z. Luo, J.J. Ge, S.N. Sun, Y.B. Chen, J. V. Hanna, S.Z. Li, X. Wang, Z.C. Xu, Navigating surface reconstruction of spinel oxides for electrochemical water oxidation, *Nat. Commun.* 14 (2023) 2467.
- [32] L.M. Deng, S.F. Hung, Z.Y. Lin, Y. Zhang, C.C. Zhang, Y.X. Hao, S.Y. Liu, C.H. Kuo, H.Y. Chen, J. Peng, J.Z. Wang, S.J. Peng, Valence oscillation of Ru active sites for efficient and robust acidic water oxidation, *Adv. Mater.* 35 (2023) 2305939.
- [33] D. Grumelli, T. Wiegmann, S. Barja, F. Reikowski, F. Maroun, P. Allongue, J. Balajka, G.S. Parkinson, U. Diebold, K. Kern, O.M. Magnussen, Electrochemical stability of the reconstructed Fe₃O₄(001) surface, *Angew. Chem. Int. Ed.* 59 (2020) 21904–21908.
- [34] J. Wang, H. Yang, F. Li, L.G. Li, J.B. Wu, S.H. Liu, T. Cheng, Y. Xu, Q. Shao, X. Q. Huang, Single-site Pt-doped RuO₂ hollow nanospheres with interstitial C for high-performance acidic overall water splitting, *Sci. Adv.* 8 (2022) eabl9271.
- [35] B. Freitas, W.G. Nunes, C.G. Real, C.B. Rodella, G. Doubek, L.M. Silva, E.H.N. S. Thaines, L.A. Pocrifka, R.G. Freitas, H. Zanin, Combining in situ electrochemistry, operando XRD & Raman spectroscopy, and density functional theory to investigate the fundamentals of Li₂CO₃ formation in supercapacitors, *J. Mater. Chem. A* 11 (2023) 20636.
- [36] W.L. Xu, W.D. Zhong, C.F. Yang, R. Zhao, J. Wu, X.K. Li, N.J. Yang, Tailoring interfacial electron redistribution of Ni/Fe₃O₄ electrocatalysts for superior overall water splitting, *J. Energy Chem.* 73 (2022) 330–338.
- [37] J.Z. He, Z.K. Ma, S.L. Liu, X.X. Qie, W.T. Zhang, Y.G. Lu, Q.L. Wu, M. Xing, Unleashing multifunctionality: Janus-structured flexible CNT-based composite film with enduring superhydrophobicity and excellent electromagnetic interference shielding, *Chem. Eng. J.* 480 (2024) 148064.
- [38] T.M. Jia, X.S. Qi, L. Wang, J.L. Yang, X. Gong, Y.L. Chen, Y.P. Qu, Q. Peng, W. Zhong, Constructing mixed-dimensional lightweight flexible carbon foam/carbon nanotubes-based heterostructures: an effective strategy to achieve tunable and boosted microwave absorption, *Carbon* 206 (2023) 364–374.
- [39] Y.L. Zhuo, D. Liu, L.L. Qiao, S.B. Chen, J.X. Lu, W.F. IP, H. Pan, Z.B. Wang, Ultrafast room-temperature synthesis of large-scale, low-cost, and highly active Ni–Fe based electrodes toward industrialized seawater oxidation, *Adv. Energy Mater.* 13 (2023) 2301921.
- [40] H.S. Hu, Z.R. Zhang, Y.W. Zhang, T.J. Thomas, H.Y. Du, K.K. Huang, J.P. Attfield, M.H. Yang, An ultra-low Pt metal nitride electrocatalyst for sustainable seawater hydrogen production, *Energy Environ. Sci.* 16 (2023) 4584–4592.
- [41] H.Y. Xue, A.L. Meng, T.Q. Yang, Z.J. Li, C.J. Chen, Controllable oxygen vacancies and morphology engineering: ultra-high HER/OER activity under base-acid conditions and outstanding antibacterial properties, *J. Energy Chem.* 71 (2022) 639–651.
- [42] Z.H. Wu, J. Shen, W.L. Li, J.S. Li, D.H. Xia, D.F. Xu, S.Y. Zhang, Electron self-sufficient core-shell BiOCl@Fe-BiOCl nanosheets boosting Fe(III)/Fe(II) recycling and synergistic photocatalysis-Fenton for enhanced degradation of phenol, *Appl. Catal. B Environ.* 330 (2023) 122642.
- [43] J. Wu, X. Wang, W.H. Zheng, Y. Sun, Y. Xie, K.K. Ma, Z. Zheng, Q.L. Liao, Z. Tian, Z. Kang, Y. Zhang, Identifying and interpreting geometric configuration-dependent activity of spinel catalysts for water reduction, *J. Am. Chem. Soc.* 144 (2022) 19163–19172.
- [44] M.M. Cai, Q. Zhu, X.Y. Wang, Z.Y. Shao, L. Yao, H. Zeng, X.F. Wu, J. Chen, K. K. Huang, S.H. Feng, Formation and stabilization of NiOOH by introducing α -FeOOH in LDH: composite electrocatalyst for oxygen evolution and urea oxidation reactions, *Adv. Mater.* 35 (2023) 2209338.
- [45] B. Zhang, Z.H. Wu, W.J. Shao, Y. Gao, W.W. Wang, T. Ma, L. Ma, S. Li, C. Cheng, C. S. Zhao, Interfacial atom-substitution engineered transition-metal hydroxide nanofibers with high-valence Fe for efficient electrochemical water oxidation, *Angew. Chem. Int. Ed.* 61 (2022) e202115331.
- [46] H.Y. Xue, T.Q. Yang, Z.M. Zhang, Y.X. Zhang, Z.H. Geng, Y. He, Stimulate the hidden catalysis potential and exposure of nickel site in NiSe@CNTs result in ultrahigh HER/OER activity and stability, *Appl. Catal. B Environ.* 330 (2023) 122641.
- [47] D.Y. Li, R. Xiang, F. Yu, J.S. Zeng, Y. Zhang, W.C. Zhou, L.L. Liao, Y. Zhang, D. S. Tang, H.Q. Zhou, In situ regulating cobalt/iron oxide-oxyhydroxide exchange by dynamic iron incorporation for robust oxygen evolution at large current density, *Adv. Mater.* (2023) 202305685.
- [48] D.X. Xu, S.R. Liu, M.Y. Zhang, L.L. Xu, H. Gao, J. Yao, Manipulating the dynamic self-reconstruction of CoP electrocatalyst driven by charge transport and ion leaching, *Small* 19 (2023) 2300201.
- [49] H. Le, L. Ma, Q.X. Wan, S.Z. Tan, B. Yang, Z.L. Wang, W.J. Mai, H.J. Fan, Promoting SUrface Reconstruction of NiFe layered double hydroxide for enhanced oxygen evolution, *Adv. Energy Mater.* 12 (2022) 2202522.
- [50] J.X. Feng, H. Xu, Y.T. Dong, S.H. Ye, Y.X. Tong, G.R. Li, Corrigendum: efficient hydrogen evolution electrocatalysis using cobalt nanotubes decorated with titanium dioxide nanodots, *Angew. Chem. Int. Ed.* 58 (2019) 12327.
- [51] H.L. Zhang, J.J. Li, Y. Chen, J.Y. Wu, K. Wang, L.J. Chen, Y. Wang, X.W. Jiang, Y. Liu, Y.L. Wu, D.Y. Jin, W.B. Bu, Magneto-electrically enhanced intracellular catalysis of FePt-FeC heterostructures for chemodynamic therapy, *Adv. Mater.* 33 (2021) 2100472.
- [52] X. Ren, T.Z. Wu, Y.M. Sun, Y. Li, G.Y. Xiang, X.H. Liu, C.M. Shen, J. Gracia, H. J. Gao, H.T. Yang, Z.C.J. Xu, Spin-polarized oxygen evolution reaction under magnetic field, *Nat. Commun.* 12 (2021) 2608.